nature communications

Article

https://doi.org/10.1038/s41467-024-54275-1

Atomically distributed Al-F_3 nanoparticles towards precisely modulating pore size of carbon membranes for gas separation

Received: 5 May 2024

Accepted: 6 November 2024

Published online: 02 January 2025

Check for updates

Xiuling Chen[1,2], Zhiguang Zhang[1], Shan Xu[1], Bin Zhang[1] ✉, Yong Qin[1], Canghai Ma[3] ✉, Gaohong He[3] ✉ & Nanwen Li[1] ✉

To confront the energy consumption, high performance membrane materials are urgently needed. Carbon molecular sieve (CMS) membranes exhibit superior capability in separating gas mixtures efficiently. However, it remains a grand challenge to precisely tune the pore size and distribution of CMS membranes to further improve their molecular sieving properties. Herein, we report an approach of finely modulating CMS pore structure by using the reactive $Al(CH_3)_3$ to in situ defluorinate the polymer precursor to form Al-$F_x(CH_3)_{3-x}$ in the polymer matrix, which is further converted to atomic-level Al_2O_3 and Al-F_3 in the polymer matrix. These nanoparticles play the key role in regulating the pore size of CMS membranes by suppressing the formation of unfavorable large pores during pyrolysis, thus enhancing the gas selectivity considerably. The resultant CMS membranes demonstrate a H_2/CH_4 and CO_2/CH_4 selectivity of 192.6, and 58.4, respectively, 128% and 93% higher than the untreated samples, residing far above the latest upper bounds.

Energy consumption associated with the separation and purification of industrial gases accounts for 10–15% of global energy use and will continue to grow to triple by 2050 with global population and economic development[1]. Compared with traditional thermally separation processes, membrane technology is economically attractive for gas separation, as it is more energy efficient with lower capital cost, smaller physical footprints and more environmental benignity than conventional thermally driven distillation processes[2–5]. Among various membrane materials, Carbon Molecular Sieve (CMS) materials have been extensively explored by thermal decomposition of polymer precursors to produce a carbon material with a dual-distribution of micropores and ultra-micropores, offering simultaneously high gas separation productivity and efficacy[6,7]. For instance, 6FDA-based polyimides have been used as precursors to fabricate CMS membranes demonstrating ultra-high gas permeability and selectivity which surpass the well-known Robeson upper bound[8–14].

In recent decades, although new structures of precursor polymers have been designed to prepare CMS membranes[15–20], it remains a crucial hurdle to precisely tune the pore size and distribution of CMS materials to further improve their molecular sieving properties. In the context, treating precursors by crosslinking or polymer blending has been explored to modulate the pore size of CMS membranes[18–25], which, however, exhibits limited ability in controlling the pore size, as reflected by the moderate enhancement of gas selectivity. As a family of high-performing materials, 6FDA-based polyimides have been heavily explored to fabricate CMS membranes since the fluorinated -CF_3 groups create a large fraction free volume, contributing the high throughputs of CMS membranes[21]. Nonetheless, the vast majority of researches focus on the pyrolysis parameters to manipulate the pore size and a thermal treatment temperature as high as 900 °C is often used to prepare selective membranes, tending to make membranes fragile and prone to breakage[19].

---

[1]State Key Laboratory of Coal Conversion, Institute of Coal Chemistry Chinese Academy of Sciences, Taiyuan, China. [2]Hubei Key Laboratory of Radiation Chemistry and Functional Materials, Hubei University of Science and Technology, Xianning, China. [3]State Key Laboratory of Fine Chemicals, Frontier Science Center for Smart Materials, School of Chemical Engineering, Dalian University of Technology, Dalian, China. ✉e-mail: zhangbin2009@sxicc.ac.cn; cma@dlut.edu.cn; hgaohong@dlut.edu.cn; linanwen@sxicc.ac.cn

In order to address the abovementioned challenges in CMS, herein, we proposed a methodology of precisely tuning CMS pore structure by using the reactive $Al(CH_3)_3$ to in situ defluorinate the 6FDA-polyimide precursor to form $Al\text{-}F_x(CH_3)_{3\text{-}x}$ intermediate (including $Al\text{-}F_3$) where x = 1, 2 or 3. Such an intermediate complex is coverted to atmoic-level Al_2O_3 and $Al\text{-}F_3$, which finely modulate the pore formation of CMS membranes. Indeed, these atomically distributed nanoparticles in the polymer matrix retard the formation of unfavorable large pores and promotes the creation of relatively small and uniform pores, thus enhancing the gas selectivity considerably without prohibitvely sacrificing the gas permeability. Specifically, in this work, we judiciously selected a F-rich 6FDA-TFDB polyimide as an exemplified 6FDA-based polymer precursor to prepare CMS membranes. As illustrated in Fig. 1, the $\text{-}CF_3$ moieties in the side chains of 6FDA-TFDB polyimide partially in situ react with $Al(CH_3)_3$ to form the defluorinated polymer, $R\text{-}CF_{(3\text{-}x)}(CH_3)_x$, and $Al\text{-}F_x(CH_3)_{3\text{-}x}$ intermediate in the polymer matrix. During the exposure of moisture, $Al\text{-}F_x(CH_3)_{3\text{-}x}$ was instantly transformed into Al_2O_3 and $Al\text{-}F_3$ in the polymer precusor. In the later pyrolysis of this hybrid precuresor, the off-gas from the decompositie of polyimide, HF, reacts with Al_2O_3 to further produce $Al\text{-}F_3$ in CMS membrane. The resultant CMS membranes demonstrate unprecedented gas separation performance well above the latest trade-off lines for gas pairs including CO_2/CH_4, H_2/CH_4, H_2/N_2, H_2/CO_2, and O_2/N_2. Moreover, the CMS membranes display significantly reduced aging compared with untreated samples. To our best knowledge, it is the first time to report the in situ formation of $Al\text{-}F_3$ in both the polymer precursor and CMS to precisely regulate the pore size of CMS with dramatically enhanced separation performance and aging resistance.

Results

Preparation and characterization of 6FDA-TFDB-x precursor and CMS membranes

The synthesis of white 6FDA-TFDB polymer was shown in Supplementary Fig. S1. Loading freshly-made pristine 6FDA-TFDB membranes in the chamber (Supplementary Fig. S2), trimethyl aluminum (TMA) and water were applied on membrane samples as vapor phase precursors for Al_2O_3 deposition[26,27], and a short exposure time of 8 s was adopted for precise control of TMA deposition on membrane surfaces and within micropores (Fig. 1). The resulting white and transparent membranes were designated as 6FDA-TFDB-x, where x refers the number of cycles of the ALD process (4–12). Afterward, the 6FDA-TFDB-x polymer membrane was pyrolyzed in a controlled environment to create CMS membranes. The pyrolysis temperature was controlled via a three-zone tube furnace at 550 °C under Ar purging. Details of the experimental method related to the fabrication of CMS membranes are described in the Supporting Information.

The physicochemical properties of membranes were first characterized. The TGA trace of 6FDA-TFDB and 6FDA-TFDB-x precursor membranes are shown in Supplementary Fig. S3. 6FDA-TFDB and 6FDA-TFDB-x precursor membranes exhibit similar trends of weight loss, suggesting the trace Al in the polymer membranes has insignificant effects in the membrane thermal stability. In addition, the surface and cross-sectional morphologies of the 6FDA-TFDB and 6FDA-TFDB-x precursor membranes were examined using SEM. As shown in Supplementary Fig. S4, the precursor membranes demonstrate rather homogeneous morphological structures. The F and Al distribution on the surface and in cross-sections of 6FDA-TFDB-x precursor and CMS membranes were analyzed by Al and F elemental SEM and EDS mapping (Supplementary Fig. S5). Apparently, the aluminum content on the surface of membrane increases with different cycles (highlighted as red spots in Supplementary Fig. S4a–d, yellow spots refer the overlap of red and green). As expected, the EDS mapping results of the cross-sectional specimen (Supplementary Fig. S4e–h) indicate that the content of aluminum increases from 4 to 7 cycles (cross-sectional specimen shown in Supplementary Fig. S6). On the other hand, the concentration of fluorine increases with the number of cycles from 7 to 12 cycles, which was due to the in situ formation of Al-F complex during the ALD and pyrolysis process[28].

The elements contents of polymer precursor membrane samples were further studied by X-ray photoelectron spectrometer (XPS) (Fig. 2 and Supplementary Figs. S7 and 8). XPS results in Fig. 2a and

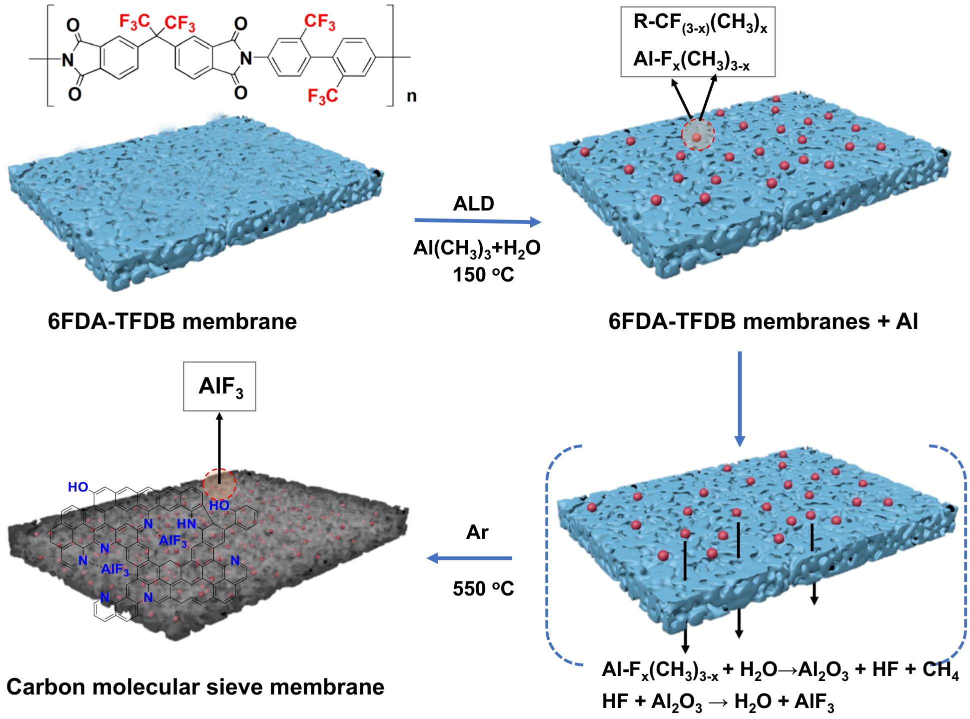

Fig. 1 | Schematic of the CMS membranes fabricated byALD strategy. Including chemical structure of 6FDA-TFDB polymer with the proposed reaction mechanism during ALD and pyrolysis process.

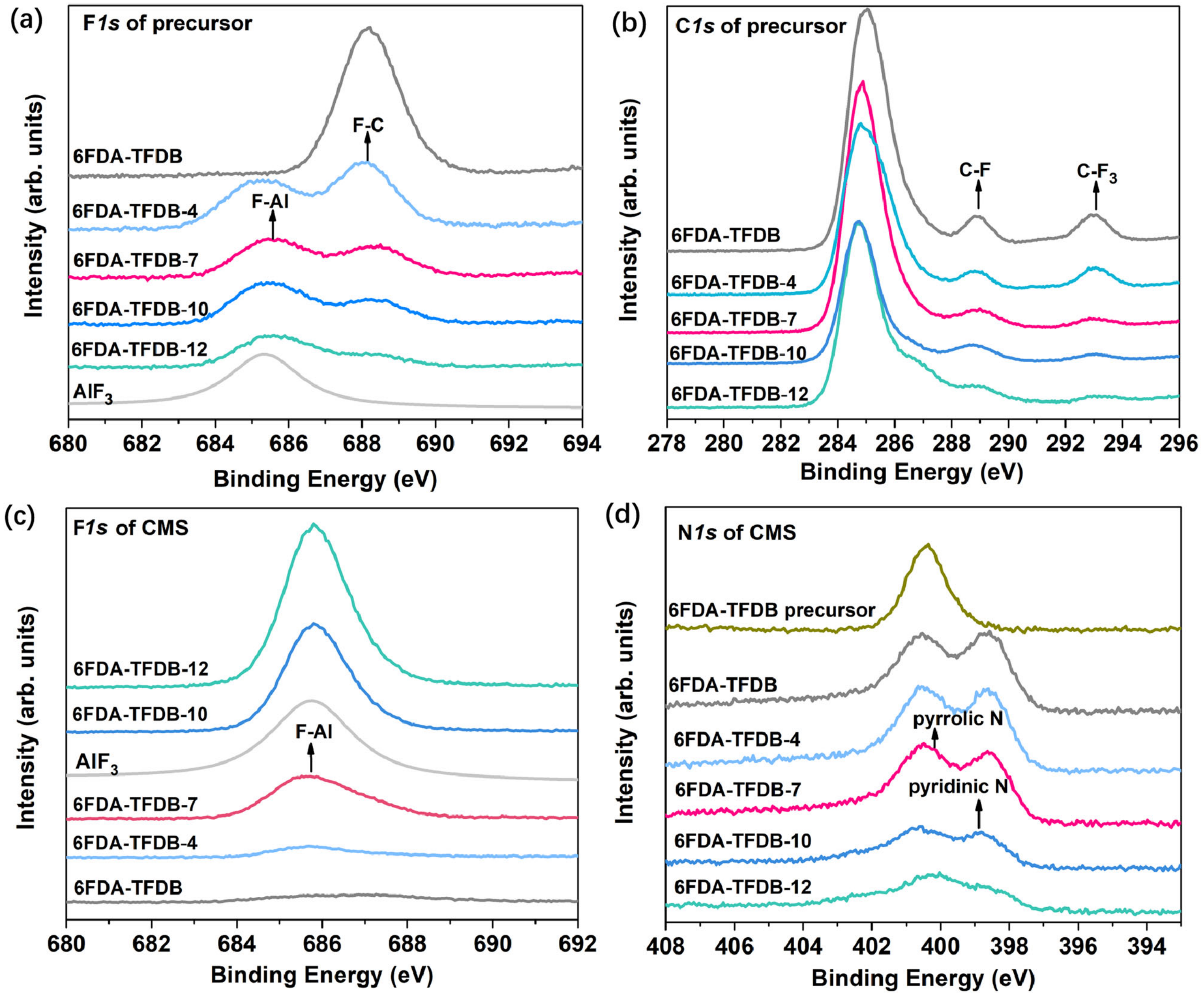

Fig. 2 | XPS characterization of 6FDA-TFDB-x precursor and CMS. a Typical F1s XPS of 6FDA-TFDB-x precursors to compare with AlF_3. **b** C1s XPS of 6FDA-TFDB-x precursors. **c** F1s of 6FDA-TFDB-x CMS membranes with AlF_3. **d** N1s of 6FDA-TFDB-x CMS membranes with 6FDA-TFDB precursor.

Supplementary Fig. S6 demonstrate that the content of F-Al in 6FDA-TFDB precursor membranes gradually increases with cycles at the peak of 685.2 eV. However, the F-C content decreases from 4 to 12 cycles at the peak of 688.1 eV. It is hypothesized that the highly reactive $Al(CH_3)_3$ could defluorinate the polymer precursor, leading to the reduction of F-C content. Such an Al-induced defluorination phenomenon of F-containing polymers was also observed in literature[29,30]. Furthermore, as the deconvoluted F1s peaks shown in Supplementary Fig. S6, the degree of F-Al area is found to increase from 39% to 74% with the cycles increasing from 4 to 12, corroborating the formation of F-Al bonds in the ALD process. On the other hand, as shown in Fig. 2b, there is a sharp decrease of C1s signal (~293.1 eV) corresponding to the CF_3 group when increasing cycles from 4 to 12, indicating that CF_3 bonds reduce with more ALD cycles, consistent with the trends shown in Fig. 2a and Supplementary Fig. S6. In addition, XPS of Al2p in 6FDA-TFDB-x precursors was conducted with results shown in Supplementary Fig. S8. The binding energy of 74.9 eV is assigned to Al-O, suggesting the formation of aluminum oxide in the membranes. Moreover, the binding energy of 76.5 eV in the Al2p spectra corresponds to Al-F with intensities of signals gradually increasing with the cycles[29,31]. Such a trend not only agrees with the result in Fig. 2a but also provides further evidence of Al-F formation upon ALD treatment.

CMS membrane samples were also characterized using XPS and the spectra exhibit distinct peaks resulting from the presence of F1s, N1s, Al2p, and C1s as shown in Fig. 2c, d and Supplementary Figs. S9 and 10. As expected, the F1s XPS spectrum of untreated 6FDA-TFDB CMS membranes shown F-C bonds at the peak of 688.1 eV, which, however, does not exhibit F-Al bonds since ALD treatment was not applied in the process of CMS fabrication (Fig. 2c). Interestingly, upon ALD treatment, F-C bonds disappear, consistent with our previous study that the ALD tends to defluorinate the precursor, essentially leading to the loss of F-C groups. Moreover, the content of F-Al as indicated by the peak at 688.1 eV increases with cycles to increase the content of aluminum in CMS membranes. On the other hand, the content of pyridinic N in CMS has been found to play a critical role in gas transport properties, and the decrease of pyridinic N reduces gas permeabilities[32]. As Fig. 2d shows, the N1s spectra clearly display the presence of both pyridinic N and pyrrolic N, corresponding to the peak at 398.0–398.8 eV and 400.3–400.8 eV, respectively. The intensities of pyridinic N and pyrrolic N peaks decrease with increased cycles. Based on the deconvoluted N1s peaks shown in Supplementary Fig. S9, the areas of pyridinic N of 6FDA-TFDB and 6FDA-TFDB-x (x = 4, 7, 10, 12) CMS membranes are estimated to be 39.4%, 39.1 %, 36.3%, 33.1% and 26.8%, respectively. The increase of cycles to reduce the contents of pyridinic N, indicating the ALD treatment affects the formation of pyridinic N during pyrolysis. In addition, Al2p XPS of 6FDA-TFDB-x CMS membranes show that Al-F content of membranes increases with the cycles (Supplementary Fig. S10), as more Al_2O_3 were converted

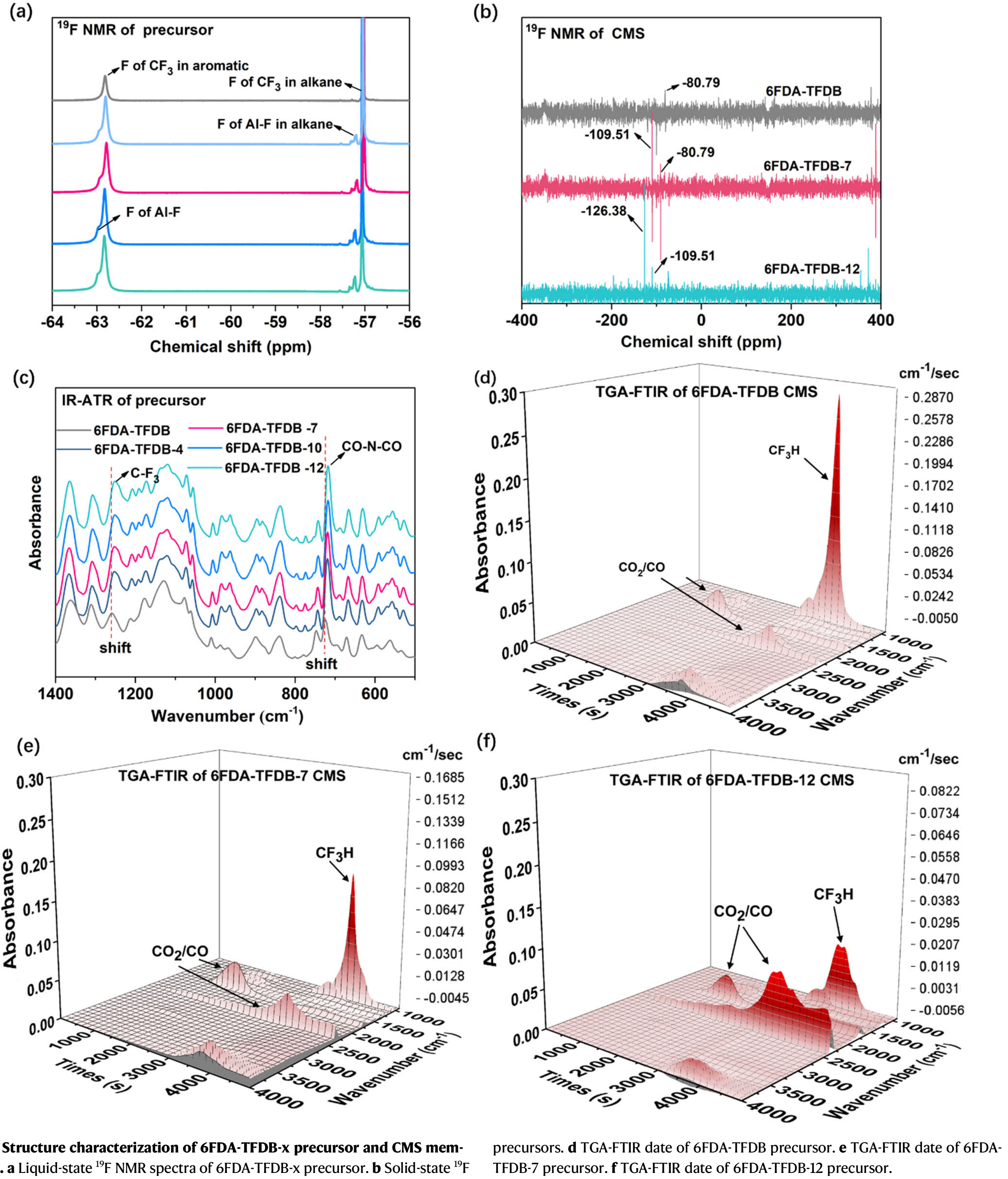

Fig. 3 | Structure characterization of 6FDA-TFDB-x precursor and CMS membranes. a Liquid-state ^{19}F NMR spectra of 6FDA-TFDB-x precursor. **b** Solid-state ^{19}F NMR of 6FDA-TFDB-x CMS. **c** Solid-state ATR-FTIR spectra of 6FDA-TFDB-x precursors. **d** TGA-FTIR date of 6FDA-TFDB precursor. **e** TGA-FTIR date of 6FDA-TFDB-7 precursor. **f** TGA-FTIR date of 6FDA-TFDB-12 precursor.

into Al-F complex[28]. Raman was also conducted on CMS membranes with the *D* and *G* peaks shown in Raman spectra (Supplementary Fig. S11). The smaller the I_D/I_G ratio, the lower the defect density in the material and the higher the graphite-like regularity[13,20]. As the ALD increase from 4 to 12 cycles, the ratio of I_D/I_G gradually decreases, indicating an increased degree of graphitization and a reduced level of defects in the amorphous CMS structure.

The evolution of chemical structure of precursors upon ALD process is further probed by ^{19}F NMR, ATR-FTIR and TGA-FTIR. As illustrated in ^{19}F NMR spectra of 6FDA-TFDB and 6FDA-TFDB-x precursors (Fig. 3a) and CMS of 6FDA-TFDB-x, aromatic and alkane C-F_3 in TFDB and 6FDA moieties are clearly detected. More importantly, an apparent new peak at ~57.2 ppm emerges, suggesting the formation of Al-F bonds. ^{19}F NMR spectra of 6FDA-TFDB-x CMS membranes show that the chemical shifts of Al-F shift from −109.51 ppm to −126.38 ppm due to terminal F atoms are highly shielded with the ALD increasing (Fig. 3b). In addition, as shown by ATR-FTIR in Fig. 3c, the peak of 1256 cm^{-1} is ascribed to C-F_3 stretching vibration of polymers[33]. Upon ALD treatment, detectable C-F_3 shifts from 1256 cm^{-1} to 1250 cm^{-1} were found in 6FDA-TFDB-x precursor membranes, which ascribe to the increased interaction between F and Al with cycles since the heavy mass Al reduces the vibration frequency of C-F_3 stretching and rocking. As TGA-FTTR results of 6FDA-TFDB-x membranes shown in Fig. 3d–f, major off-gases including CO_2, CO and CF_3H were released during the pyrolysis, consistent with the literature reported elsewhere[20]. Moreover, the amount of CF_3H gas tends to decrease when the ALD cycles increase from 4 to 12, as indicated by the TGA-FTIR spectra data, likely due to partial -CF_3 groups transformed into AlF_3, consistent with the EDS mapping results in Supplementary Fig. S4. CMS membrane samples were also tested using ATR-FTIR with results shown in Supplementary Fig. S12b, which display broad shoulders of absorbance peaks at ~890–1145 cm^{-1}, corresponding to Al-F stretching vibrations[34,35]. The occurrence of absorbance peaks of Al-F_3 in a broad range of vibrational frequencies again confirms the formation of Al-F bonds[36].

To further illustrate the critical role of Al-F bonds formed in situ during ALD treatment, we prepared CMS membranes by mixing precursor polymers with 2% and 5% Al_2O_3 particles, following by pyrolysis with same conditions as ALD treated samples. XPS (Supplementary Figs. S13–16) was performed on both precursors and CMS membranes. The Al2p XPS and F1s XPS results do not reveal the F-Al bond in the 6FDA-TFDB/Al_2O_3 precursor or CMS membranes (Supplementary Figs. S13 and 14), since the peaks of binding energy completely differ from the Al-F bond as demonstrated in samples with ALD treatment (Fig. 3a, Supplementary Figs. S7 and 8). In addition, C1s XPS results show that the C-F bond was not impacted by the addition of Al_2O_3 in precursors as the intensities of binding energy remain similar for polymer and Al_2O_3-doped polymer membranes (Supplementary Fig. S15), different from membranes with ALD cycles (Fig. 2b). In a sharp contrast to the case of ALD-treated membranes, the N1s spectra of 6FDA-TFDB/Al_2O_3 CMS membranes show the same ratio of pyridinic N and pyrrolic N while such ratio in 6FDA-TFDB CMS membranes changes significantly with different ALD cycles (Supplementary Figs. S9 and S16). The above characterization proves that Al-F bond cannot be established by simply mixing Al_2O_3 with -CF_3 containing polymers, reflecting the crucial role of ALD treatment in creating Al-F bonds in membranes.

The research of gas sorption and pore sizes

The gas sorption and pore sizes of CMS membranes were analyzed with N_2 adsorption experiments. As shown in Fig. 4a, the N_2 adsorption capacity drops as the number of cycles increases, owing to the pore-blocking effect of ALD treatments with added cycles. As a result, the N_2 derived BET surface area decreases from 949.8 to 847.6 m^2 g^{-1} for the 6FDA-TFDB and 6FDA-TFDB-12 CMS membranes, respectively (Supplementary Table S1). The pore size distributions of CMS membranes were further examined based on non-local density functional theory with results illustrated in Fig. 4b, showing that the 6FDA-TFDB CMS membrane possesses an average pore size of 6–11 Å. In contrast, after 4–12 cycles, the average pore size decreases to the range of 5.5–8.0 Å. The 6FDA-TFDB-x CMS membranes show a clearly reduced pore size compared to the pristine 6FDA-TFDB CMS membrane, suggesting that ALD treatment is expected to enhance molecular sieving properties of CMS membranes by narrowing the pore sizes and creating ultramicropores in CMS matrix as will be discussed later.

Pure and mixed gas separation performance

To study effects of ALD on membrane separation performance, the gas permeability and selectivity of both precursors and CMS membranes derived from 6FDA-TFDB and 6FDA-TFDB-x were tested with permeation results summarized in Supplementary Table S1-2, Fig. 4 and Supplementary Fig. S17. The results of polymeric precursors in Fig. 4c, d shows that the gas permeability decreases continuously while the selectivity generally decreases with the increase of cycles. ALD deposition layer near the surface of membranes creates additional gas transport resistance, thereby reducing the gas permeabilities, which, however, does not improve molecular sieving properties of polymeric membranes. Surprisingly, 6FDA-TFDB-x CMS membranes show pronounced enhancement of gas selectivities upon ALD treatment. Similar to polymeric precursors, the more cycles and the lower gas permeabilities of CMS membranes. The drop of permeability results from the additional layer by ALD deposition and consistent with the decrease of content of pyridinic N as shown in Fig. 2d, which also agrees with the finding reported in the literature[32]. On the other hand, the effect of ALD on gas selectivity is relatively complicated. In the beginning, the gas selectivity of 6FDA-TFDB-x CMS membranes is amplified by introducing cycles from 4 to 7 with a drop of gas permeability. For instance, 6FDA-TFDB-7 shows a CO_2/CH_4 selectivity of 58.4 with a CO_2 permeability of 7767 Barrer, compared with a CO_2/CH_4 selectivity of 30.2 and a CO_2 permeability of 12653 Barrer in the case of untreated 6FDA-TFDB CMS membranes. Higher pyrolysis temperatures up to 800 °C were also investigated with gas permeation shown in Supplementary Table S2 and XPS results shown in Supplementary Fig. S20. The 6FDA-TFDB and 6FDA-TFDB-7 CMS membranes pyrolyzed at 700 °C display lower CO_2 permeability but higher CO_2/CH_4 selectivity compared with the cases of 550 °C pyrolysis. An increase in pyrolysis temperature to 800 °C led to higher CO_2/CH_4 selectivity but lower CO_2 permeability compared with that of 700 °C. The 6FDA-TFDB-7 CMS membrane pyrolyzed at 800 °C show attractive performance with a CO_2 permeability of 1805 Barrer and a CO_2/CH_4 selectivity of 189.5.

By plotting with upper bounds, the overall performance of 6FDA-TFDB-4 and 6FDA-TFDB-7 CMS surpass the latest upper bounds for CO_2/CH_4 and O_2/N_2 (Fig. 4e, f). In fact, the CO_2/CH_4 selectivity of 6FDA-TFDB-7 CMS membranes is the highest among reported 550 °C pyrolyzed CMS membranes derived from polymers including Matrimid®, 6FDA-BPDA/DAM, 6FDA-mPDA/DABA, 6FDA/DETDA-DABA, 6FDA/1,5-ND:ODA,TB, PIM, and PIM-PI, as shown in Supplementary Table S4 and other polymers[37,38]. When further increasing the number of cycles to 10 and 12, the gas selectivity of CMS membranes tends to decrease but remains higher than untreated membranes. In any case, the above results suggest that ALD strategy is an effective strategy in developing CMS membranes with high permeability and selectivity and there exists an optimal cycle for preparing the most selective CMS materials. Presumably, the existence of Al-F complex plays the key role in affecting CMS membrane separation performance, generated from two possible paths: 1) defluorination of polymer precursors with $Al(CH_3)_3$ during ALD treatment in the absence of pyrolysis; 2) reaction of Al_2O_3 with HF released during pyrolysis starting at a temperature of ~450 °C[39]. Al-F complex is expected to interact strongly with strands including -C=O[40], C-N[41] and C-F moieties by Vander Waals force during pyrolysis, which likely promotes an efficient packing of strands and reduces the pore sizes, essentially improving the gas selectivity. However, when excessive cycles applied, the pore size reduces to a level where the fast gas permeability (i.e. H_2, CO_2) drops more rapidly than the slow gas (i.e. N_2, CH_4), leading to a decrease of gas selectivity.

In order to decouple the effect of Al-F from Al_2O_3 on gas separation performance, 1%, 2%, 4% and 5% Al_2O_3 and AlF_3 were blended with 6FDA-TFDB to prepare mixed matrix membranes, followed by pyrolysis to fabricate CMS membranes. The optical images of mixed matrix membranes incorporated with Al_2O_3 or AlF_3 are opaque, different from transparent 6FDA-TFDB-x samples with the ALD process (Supplementary Fig. S18). In addition, the mechanical properties of mixed matrix membranes CMS are relatively lower than the 6FDA-TFDB and 6FDA-TFDB-x CMS membranes (Supplementary Fig. S19).

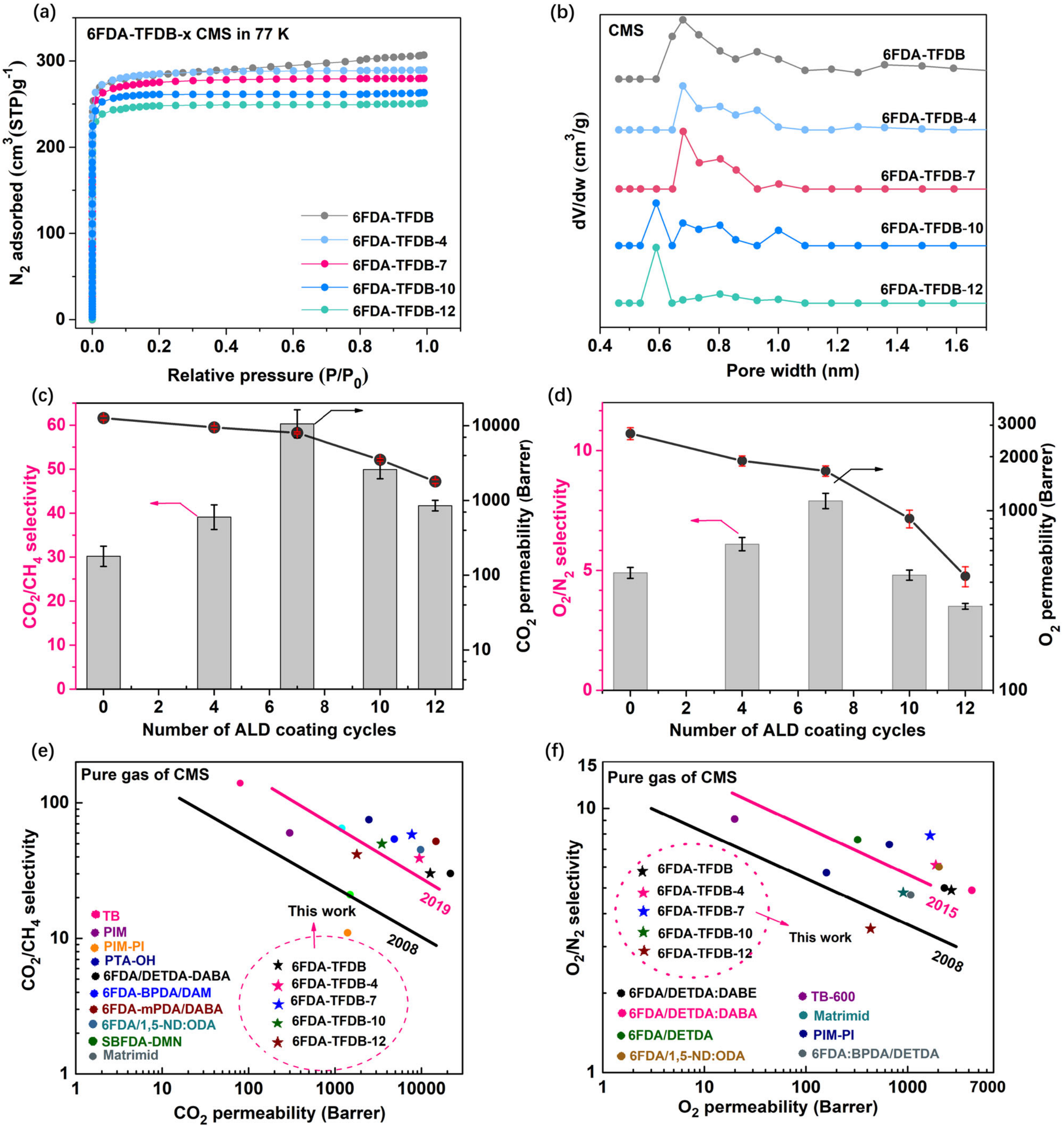

Fig. 4 | The pore size characterization and gas separation performances of 6FDA-TFDB-x CMS membranes. **a** N_2 adsorption isotherms of 6FDA-TFDB-x CMS membranes was obtained at 77 K. **b** Pore size distribution of 6FDA-TFDB-x CMS membranes from N_2 adsorption. **c** CO_2 permeability and CO_2/CH_4 selectivity of 6FDA-TFDB-x CMS membrane. **d** O_2 permeability and O_2/N_2 selectivity of 6FDA-TFDB-x CMS membrane. **e** The latest 2019 upper bound of CO_2/CH_4, **f** the latest of 2015 upper bound of O_2/N_2. The error bars in **c** and **d** represent standard deviation.

Furthermore, the gas separation performance of those membranes was tested with results shown in Supplementary Table S2. As a typical pore former, the addition of Al_2O_3 improves the gas permeability with a simultaneous loss of gas selectivity. However, in the case of AlF_3 mixed matrix membranes, AlF_3 tends to reduce gas permeability and increase gas selectivity in a strong agreement with aforementioned discussions. For instance, 5 wt% AlF_3 6FDA-TFDB CMS membranes display an increase of CO_2/CH_4 selectivity from 30.2 to 42.6, and O_2/N_2 selectivity from 4.9 to 5.6, compared with untreated 6FDA-TFDB CMS, respectively. These experiments further corroborate our findings on the crucial role of the Al-F bond in determining CMS structures and molecular sieving properties, in addition, the Al element was distributed uniformly in 6FDA-TFDB-x membrane, as confirmed by SEM-EDX mapping and TEM (Supplementary Figs. S21–S24).

The gas separation performance of 6FDA-TFDB and 6FDA-TFDB-7 CMS membranes under high operation pressures was explored using a binary mixture of CO_2/CH_4 and CO_2/N_2 (50/50 vol.%). As shown in Fig. 5 and Supplementary Fig. S16, the CMS membranes demonstrate excellent CO_2/CH_4 mixed-gas separation performance at elevated pressures. The CO_2/CH_4 mixed-gas selectivity reaches as high as 55.6 at

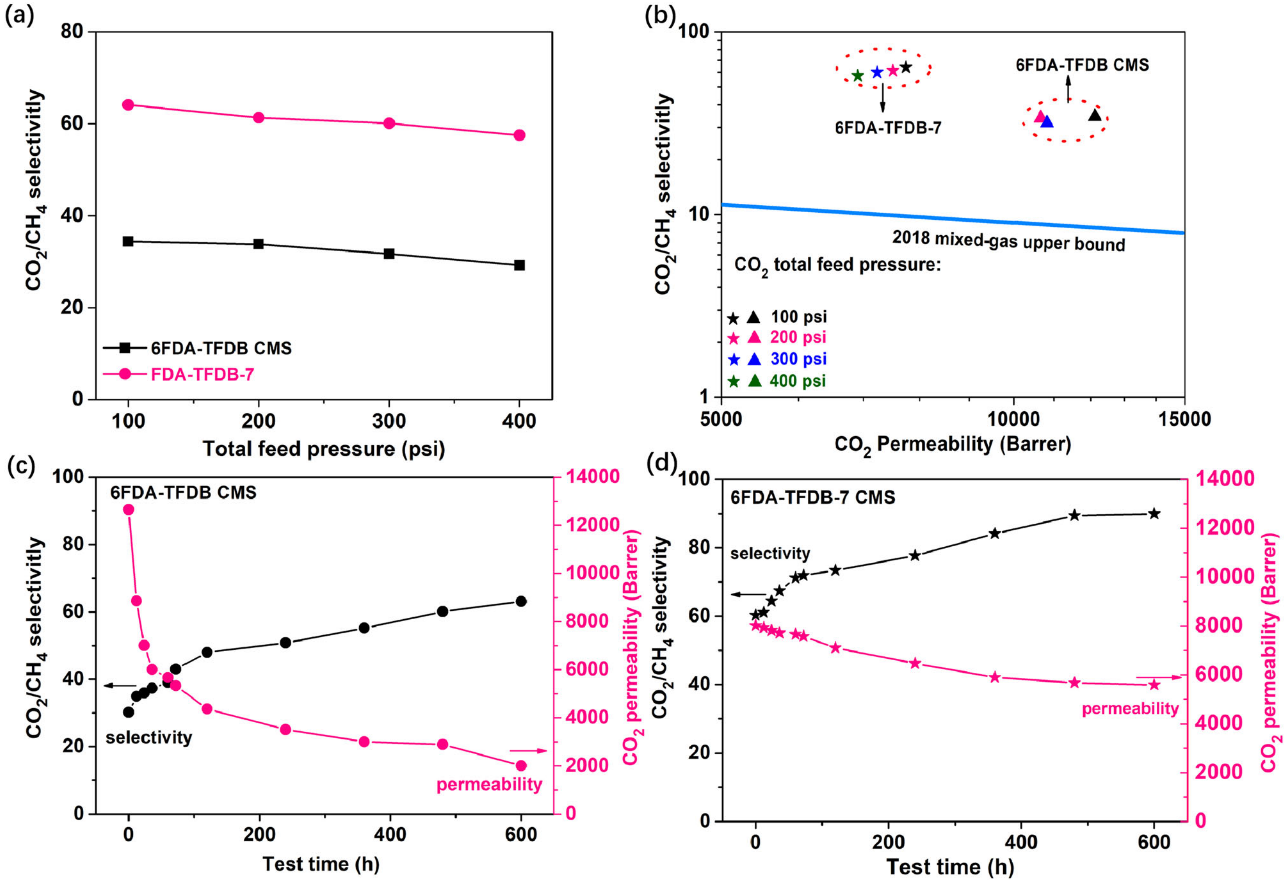

Fig. 5 | Gas separation performances of mixed gas, anti-plasticization and aging performance. a 50%/50% CO_2/CH_4 mixed-gas separation performance at different CO_2 upstream partial pressures ranging from 100 to 400 psi. **b** The upper bound of mixed-gas with 6FDA-TFDB and 6FDA-TFDB-7 CMS membranes. **c** Physical aging behavior of the 6FDA-TFDB CMS membrane over time. **d** Physical aging behavior of the 6FDA-TFDB-7 CMS membrane over time.

a feed pressure of 400 psi. Moreover, the CO_2/CH_4 selectivity of 6FDA-TFDB and 6FDA-TFDB-7 CMS membranes maintain nearly unchanged comparing with the pure gas permeation results (Fig. 5a). Such mixed gas separation performance places the CMS membranes well above the mixed-gas trade-off curve for CO_2/CH_4 (Fig. 5b). Furthermore, the CO_2/N_2 selectivity of 6FDA-TFDB without ALD treatment was lower than 2019 upper bound while 6FDA-TFDB-7 CMS membranes with ALD treatment surpass the 2019 upper bound, indicative of the critical role of ALD treatment in affecting the membrane separation performance.

The aging behavior of 6FDA-TFDB and 6FDA-TFDB-7 CMS membranes

A key obstacle for most CMS membranes lies in their lack of long-term stability[42,43]. To investigate the durability of 6FDA-TFDB and 6FDA-TFDB-7 CMS membranes over time, we performed an aging study as long as 480 h, during which the upstream and downstream of membrane samples were pulling vacuum with results shown in Fig. 5 and Supplementary Table S3. Similar to other reported CMS, the untreated 6FDA-TFDB CMS membrane shows a typical physical aging phenomenon and the CO_2 permeability drops over 70.3% from 12,653 to 3764 Barrer during the first 120 h (Fig. 5c, d). The aging tends to slow down after 120 h but there is still a drop of CO_2 permeability over 30% during aging from 120 → 480 h. In a sharp contrast, the ALD treated 6FDA-TFDB-7 CMS membranes demonstrate significantly enhanced aging resistance. The CO_2 permeability decreases only 13.6% from 7767 to 6709 Barrer during the first 120 h aging, much lower than the case of untreated CMS. After aging for 120 h, the CO_2 permeability of 6FDA-TFDB-7 decrease 10.3%. Combing the two stages of aging, the ALD treated CMS samples only show a loss of CO_2 permeability less than 13.6%, considerably lower than that in the case of untreated CMS (i.e. 70.3%). On the other hand, both CMS samples exhibit pronounced increases of gas selectivity after aging. Note that the CO_2/CH_4 selectivity of 6FDA-TFDB-7 CMS membrane is as high as 93.9 after aging 480 h. We hypothesize that the existence of the F-Al complex in the 6FDA-TFDB-7 CMS membranes results in rigidified CMS matrix, thereby suppressing the pore collapse of membranes and retaining high gas permeability during aging.

Discussion

In summary, we successfully exploited Al-F in situ formation at atomic-level to precisely tune the pore size and distribution of 6FDA-TFDB CMS membranes to further improve their molecular sieving properties. During the ALD treatment, $Al(CH_3)_3$ to defluorinate the 6FDA-TFDB polymer precursor in situ to form $Al\text{-}F_x(CH_3)_{3\text{-}x}$ then to Al_2O_3 and $Al\text{-}F_3$ in the polymer matrix as confirmed by characterizations including XPS, ATR-FTIR and ^{19}F NMR, the thermally treated at 550 °C for 2 h, all $Al\text{-}F_3$ formation on the CMS. The AlF_3-tailored ultramicropore size distribution shifted from 5.5 to 8.0 Å, which fits well for discriminating H_2 CO_2 CH_4 gases, provides an effective approach to regulate the nanopores of CMS materials and produce high-efficiency CMS with aging drastically suppressed and performance far beyond current upper bounds. With both pure- and mixed-gas permeation, the ALD treated 6FDA-TFDB-7 CMS membrane exhibits unprecedented separation performance for H_2/CH_4, CO_2/CH_4 and O_2/N_2, locating far above the latest trade-off lines. Moreover, the 6FDA-TFDB-7 CMS membrane shows significantly retarded physical aging with a CO_2 permeability loss only 22.5% during the 480 h aging study. The ALD approach described in this work offers an efficient and facile method for tailoring membrane structure and properties with potential for gas separations such as CO_2 removal and H_2 purification.

Methods

Materials

The raw material 4,4′-(hexafluoroisopropylidene)diphthalic anhydride (6FDA) and 2,2′-bis(trifluoromethyl)-[1,1′-biphenyl]-4,4′-diamine (TFDB) for the synthesis polyimide were obtained from Sigma-Aldrich and purified by sublimation prior to use. The solvent *N*-methylpyrrolidone (NMP) was dried by standard methods before using. Acetic anhydride, 2-methylpyridine, Al_2O_3, AlF_3 were obtained from Energy Chemical, and used without further purified.

Synthesis of 6FDA-TFDB polymer

The 2,2′-bis(trifluoromethyl)-[1,1′-biphenyl]-4,4′-diamine (TFDB 10 mmol) was dissolved in NMP (15 mL) under a nitrogen atmosphere. The system was stirred at −5 °C temperature for 30 min, 4,4′-(hexafluoroisopropylidene)diphthalic anhydride (6FDA 10 mmol) was added (divided into two times) and stirred for 24 h to form a polyamic acid solution. Acetic anhydride (100 mmol) and 2-methylpyridine (10 mmol) were added to polyamic acid solution and stirred for 24 h. The resulting polyimide were precipitated with methanol and washed with methanol three times at 60 °C, then dried at 80 °C under vacuum for 24 h for using (Supplementary Fig. S1). The molecular weight was estimated with the results of $M_w = 10.8 \times 10^4$, PDI = 3.4.

6FDA-TFDB membrane preparation

Dense membranes were prepared by solution casting of filtered 6FDA-TFDB in NMP on clean glass substrate inside a vacuum drying oven evaporate the solvent at 80 °C for 12 h. After completion of the evaporation of NMP solvent, the membrane was soaked in methanol for overnight and further dried in a vacuum oven at 70 °C for 24 h. The thickness of the 6FDA-TFDB membrane was about 60 μm (±10 um).

Preparation of 6FDA-TFDB-x

6FDA-TFDB-x was obtained by depositing Al_2O_3 on 6FDA-TFDB by ALD method in a custom-made hot-wall closed chamber-type ALD reactor, and the Al_2O_3 was deposited at 125 °C using trimethylaluminium (TMA) and deionized H_2O as precursors, the mechanism and detailed set-up were shown in the below Supplementary Fig. S2. The detailed Al_2O_3 ALD process contains the following steps: (i) The 6FDA-TFDB membranes with diameter of ~7 cm and thickness of ~60 μm involved placing (but not fixing) them in the ALD device, which was then pumped down under an oil pump to the pressure ~20 Pa. (ii) TMA vapor pulse was introduced to the system by opening the valve A (Supplementary Fig. S2a) for 0.02 s, which was then exposed to 6FDA-TFDB membrane for 8 s to accommodate the TMA on the surface or inside the micropore of 6FDA-TFDB, and thereafter, the system was purged with inert N_2 for 25 s to get rid of the residual non-anchored TMA in the chamber. (iii) H_2O as the second precursor was then loaded following the same procedure as that of TMA with the pulse, exposure and purge time of 0.1, 8, and 25 s, respectively. (iv) The above (ii) and (iii) procedures were repeated for different cycles to get the resulting polymer membranes. Meanwhile, membrane with 1 cm^2 was cut by scissor for gas separation testing. Membrane with each ALD cycles was tested for three different samples, and the deviation of the results was less than 5%.

Preparation of 6FDA-TFDB-x CMS membranes

The 6FDA-TFDB-x CMS membranes were obtained by pyrolyzing the6FDA-TFDB-x precursor membranes using the following procedure. More specifically, the polymer films were cut into a rectangle of 1 cm × 5 cm, and placed into a tube furnace (Centurion NeytechQex). The tube furnace was blown via Ar for 2 h, while the oxygen level was kept to be below 10 ppm as detected by using an oxygen analyser (Cambridge Sensotec Ltd, Rapidox 2100 series, Cambridge, England).

1. Starting point at 30 °C;
2. From 30 °C to 250 °C at a ramp rate of 13.33 °C/min;
3. From 250 °C to 535 °C at a ramp rate of (3.85 °C/min);
4. From 535 °C to 550 °C at a ramp rate of (0.25 °C/min);
5. Soaked at 550 °C for 120 min;
6. Cooled to the temperature of 20 °C for 180 min.

Finally, the obtained 6FDA-TFDB CMS dense membranes were carefully removed from the tube furnace to be tested.

Preparation of 6FDA-TFDB-Al_2O_3-x and 6FDA-TFDB-AlF_3-x MMMs

Specifically, Al_2O_3 and AlF3 were added to 6FDA-TFDB solution to form 2 wt% and 5 wt% solutions by physical blending and casting method. The casting solutions were stirred for 12 h and stood still for another 12 h for thorough dispersion and bubble removal before casting. Then, the solutions were cast on the glass support followed by being dried at 80 °C and for 24 h to obtain the 6FDA-TFDB-Al_2O_3-x and 6FDA-TFDB-AlF_3-x MMMs.

Gas permeability testing

The pristine and Al_2O_3 ALD modified 6FDA-TFDB dense membranes were tested in pure gas systems. The pure gas permeation properties were evaluated by a constant-volume/variable-pressure method (constant downstream volume permeation apparatus). The downstream pressure was measured using an inficon transducer ranging from 0 to 10 torr, and the steady state pressure changing with time (dp/dt) was selected to calculate the permeability (P). Each pure gas was tested in the sequence of CH_4, N_2, O_2, CO_2 and H_2, at 35 °C and 100 psi. Membranes with each ALD cycles were tested for three different samples and the deviation was less than 5%. Permeability (P) was calculated using the following Eq. (1):

$$P = \left(\frac{273}{T}\right)\left(\frac{\mathrm{dp}}{\mathrm{dt}}\right)\left(\frac{l}{\Delta pA}\right) \tag{1}$$

where P is the permeability (Barrer), 1 Barrer = 10^{-10} cm^3(STP) cm cm^{-2} s^{-1} $cmHg^{-1}$, l is the membrane thickness (cm), A is the effective membrane area (cm^2), T is the operating temperature (K), R is the gas constant (0.278 cm^3 cmHg cm^{-3}(STP) K^{-1}) and dp/dt is the steady-state downstream pressure increase rate (cmHgs^{-1}).

The ideal selectivity ($\alpha_{x/y}$) for components x and y was defined as the ratio of gas permeability of the two components via Eq. (2).

$$\alpha_{x/y} = \frac{P_x}{P_y} \tag{2}$$

Binary gas mixtures testing

The CO_2/CH_4 and CO_2/N_2 mixed-gas testing was performed at 35 °C use a gas mixture as feed gas with component ratio of 50/50, and the upstream pressure ranging from 50 to 400 psi. The retention flow rate was controlled by MFC to be ~100 times higher than the permeate gas to keep the constant component ratio in the upstream. The permeated gas was collected in the downstream volume till the pressure reached more than 9 torr. The component ratio of the permeate gas was tested and confirmed by GC (GC-7820A, Agilent). The permeability in the mixed-gas separation was calculated from the steady state using the following equation:

$$P_x = 10^{10} \times \frac{y_x \times V \times l}{x_x \times f_{upx} \times T \times R \times A} \times \frac{d_p}{d_t} \quad (3)$$

$$P_y = 10^{10} \times \frac{y_y \times V \times l}{x_y \times f_{upy} \times T \times R \times A} \times \frac{d_p}{d_t} \quad (4)$$

Where x_x and x_y are the feeding component ratio of CO_2, CH_4 or N_2 y_x and y_y are the permeate gas concentration of CO_2 and CH_4 or N_2, respectively. f is the fugacity of the upstream partial pressure, and the dp/dt is the steady-state downstream pressure increase rate (cmHg s^{-1}). The selectivity of x/y can be calculated as follows:

$$\alpha_{x/y} = \frac{y_{x/} y_y}{x_x / x_y} \quad (5)$$

Data availability

All data supporting the results of this study are available from the corresponding author upon request.

References

1. Sholl, D. S. & Lively, R. P. Seven chemical separations to change the world. *Nature* **532**, 435–437 (2016).
2. Li, Y. & Jiang, Z. Facilitated transport of small molecules and ions for energy-efficient membranes. *Chem. Soc. Rev.* **44**, 103–118 (2015).
3. Koros, W. J. Evolving beyond the thermal age of separation processes: membranes can lead the way. *AIChE J.* **50**, 2326–2334 (2004).
4. Koros, W. J. & Lively, R. P. Water and beyond: expanding the spectrum of large-scale energy efficient separation processes. *AIChE J.* **58**, 2624–2633 (2012).
5. Lively, R. P. & Sholl, D. S. From water to organics in membrane separations. *Nat. Mater.* **16**, 276–279 (2017).
6. Rungta, M. & Koros, W. J. Carbon molecular sieve structure development and membrane performance relationships. *Carbon* **115**, 237–248 (2017).
7. Wenz, G. B. & Koros, W. J. Tuning carbon molecular sieves for natural gas separations: A diamine molecular approach. *AIChE J.* **63**, 751–760 (2017).
8. Fu, S. & Koros, W. J. The significance of entropic selectivity in carbon molecular sieve membranes derived from 6FDA/DETDA:-DABA(3:2) polyimide. *J. Membr. Sci.* **539**, 329–343 (2017).
9. Salleh, W. N. W. & Abdullah, M. S. Precursor selection and process conditions in the preparation of carbon membrane for gas separation: A Review. *Separation Purification Rev.* **40**, 261–311 (2011).
10. White, H. D. & Lively, R. P. Tailoring the structure of carbon molecular sieves derived from an aromatic polyamide. *Ind. Eng. Chem. Res.* **61**, 5314–5323 (2022).
11. Sanyal, O. & Koros, W. J. A self-consistent model for sorption and transport in polyimide derived carbon molecular sieve gas separation membranes. *Angew. Chem. Int. Ed.* **132**, 20523–20527 (2020).
12. Li, L. & Wang, T. A review on the progress in nanoparticle/C hybrid CMS membranes for gas separation. *Membranes* **8**, 134 (2018).
13. Karunaweera, C. & Ferraris, J. P. Fabrication and characterization of aging resistant carbon molecular sieve membranes for C3 separation using high molecular weight crosslinkable polyimide, 6FDA-DABA. *J. Membr. Sci.* **581**, 430–438 (2019).
14. Chen, C. & Koros, W. J. Ultraselective carbon molecular sieve membranes with tailored synergistic sorption selective properties. *Adv. Mater.* **29**, 1701631 (2017).
15. Ma, X. & Pinnau, I. Carbon molecular sieve gas separation membranes based on an intrinsically microporous polyimide precursor. *Carbon* **62**, 88–96 (2013).
16. Park, H. B. & Lee, Y. M. Relationship between chemical structure of aromatic polyimides and gas permeation properties of their carbon molecular sieve membranes. *J. Membr. Sci.* **229**, 117–127 (2004).
17. Ma, Y. & Lively, R. P. Creation of well-defined "mid-sized" micropores in carbon molecular sieve membranes. *Angew. Chem. Int. Ed.* **58**, 13259–13265 (2019).
18. Oh, B. & Koh, D. Electron-mediated control of nanoporosity for targeted molecular separation in carbon membranes. *Nat. Commun.* **13**, 4972 (2022).
19. Hazazi, K. & Pinnau, I. Precise molecular sieving of ethylene from ethane using triptycene-derived submicroporous carbon membranes. *Nat. Mater.* **22**, 1218–1226 (2023).
20. Liu, Z. & Koros, W. J. Advanced carbon molecular sieve membranes derived from molecularly engineered cross-linkable copolyimide for gas separations. *Nat. Mater.* **22**, 109–116 (2023).
21. Sanyal, O. & Koros, W. J. Next generation membranes using tailored carbon. *Carbon* **127**, 688–698 (2018).
22. Chen, X. & Li, N. Small molecule DOPO-*p*-DP crosslinked 6FDA-DAM-Br-85% carbon molecular sieve membrane with superior aging for efficient gas separation. *J. Membr. Sci.* **687**, 122072 (2023).
23. Ogieglo, W. & Pinnau, I. Nanohybrid thin-film composite carbon molecular sieve membranes. *Materials Today Nano* **9**, 100065 (2020).
24. Low, B. T. & Chung, T. S. Carbon molecular sieve membranes derived from pseudo-interpenetrating polymer networks for gas separation and carbon capture. *Carbon* **49**, 2104–2112 (2011).
25. Qiu, W. & Koros, W. J. Gas separation performance of carbon molecular sieve membranes based on 6FDA-mPDA/DABA (3:2) polyimide. *ChemSusChem* **7**, 1186–1194 (2014).
26. Ge, H. & Qin, Y. A tandem catalyst with multiple metal oxide interfaces produced by atomic layer deposition. *Angew. Chem. Int. Ed.* **128**, 7197–7201 (2016).
27. Chen, X. & Li, N. Tailoring the microporosity of polymers of intrinsic microporosity for advanced gas separation by atomic layer deposition. *Angew. Chem. Int. Ed.* **60**, 17875–17880 (2021).
28. Romero, N. & Etienne, M. Regioselective C-F bond activation/C-C bond formation between fluoropyridines and cyclopropyl groups at zirconium. *Organometallics* **39**, 2245–2256 (2020).
29. Senkevich, J. J. & Weise, M. T. Stability of fluorinated parylenes to oxygen reactive-ion etching under aluminum, aluminum oxide, and tantalum nitride overlayers. *J. Electron. Mater.* **32**, 925–931 (2003).
30. Shi, K. & Yelon, A. Metallization of Teflon PFA. I. Interactions of evaporated Cr and Al measured by x-ray photoelectron spectroscopy. *J. Vac. Sci. & Technol.* **12**, 29–34 (1994).
31. Sen, F. G. & Alpas, A. T. Material transfer mechanisms between aluminum and fluorinated carbon interfaces. *Acta Materialia* **59**, 2601–2614 (2011).
32. Qiu, W. & Koros, W. J. Key features of polyimide-derived carbon molecular sieves. *Angew. Chem. Int. Ed.* **60**, 22322–22331 (2021).
33. Zhang, L. & Oh, C. F. Infrared absorption enhancement of fluorinated poly-acrylate thin films on Co-alloy substrate. *Surf. Interface Anal.* **38**, 949–956 (2006).
34. Lee, Y. & George, S. M. Atomic layer deposition of AlF_3 using trimethylaluminum and hydrogen fluoride. *J. Phys. Chem. C.* **119**, 14185–14194 (2015).
35. Lee, Y. & George, S. M. Atomic layer etching of AlF_3 using sequential, self-limiting thermal reactions with $Sn(acac)_2$ and hydrogen fluoride. *J. Phys. Chem. C.* **119**, 25385–25393 (2015).
36. Gross, U. & Harrison, N. Vibrational analysis study of aluminum trifluoride phases. *J. Phys. Chem. A.* **111**, 5813–5819 (2007).

37. Genduso, G. & Pinnau, I. Carbon molecular sieve gas separation materials and membranes: A comprehensive review. *J. Membr. Sci.* **699**, 122533 (2024).
38. Hardian, R. & Szekely, G. Nanodomain control in carbon molecular sieve membranes via nanomaterial footprinting. *Small Sci*. **24**, 230016 (2024).
39. Cochran, C. N. Recovery of hydrogen fluoride fumes on alumina in aluminum smelting. *Environ. Sci. Technol.* **8**, 63–66 (1974).
40. Pelissier, B. & Joubert, O. HF contamination of 200 mm Al wafers: a parallel angle resolved XPS study. *Microelectronic Engineering* **88**, 861–866 (2011).
41. Shetty, D. & Chung, Y. K. Stable aluminum fluoride chelates with triazacyclononane derivatives proved by X-ray crystallography and 18 F-labeling study. *Chem. Commun.* **47**, 9732–9734 (2011).
42. Hays, S. S. & Koros, W. J. Envisioned role of slit bypass pores in physical aging of carbon molecular sieve membranes. *Carbon* **157**, 385–394 (2020).
43. Xu, L. & Koros, W. J. Physical aging in carbon molecular sieve membranes. *Carbon* **80**, 155–166 (2014).

Acknowledgements

Financial support was from the National Natural Science Foundation of China (NO. 22378102, Innovative Research Group 22021005, 22378039, 22141001) and the Fundamental Research Funds for the Central Universities (DUT22LAB603).

Author contributions

Xiuling Chen and Zhiguang Zhang contribute equally to this text. X.C. and Z.Z conceived the research, performed the experiments, analyzed the data, and have written the paper. S.X. contributed to polymer and mixed-gas permeation; B.Z. and Y.Q. assisted in ALD experiments and analyzed the data. N.L., C.M. and G.H provided new insights into the research, guided the project, supervised the work. All authors contributed to the manuscript.

Competing interests

The authors declare no competing interests.

Additional information

Supplementary information The online version contains supplementary material available at https://doi.org/10.1038/s41467-024-54275-1.

Correspondence and requests for materials should be addressed to Bin Zhang, Canghai Ma, Gaohong He or Nanwen Li.

Peer review information *Nature Communications* thanks Suzana Nunes and the other, anonymous, reviewer(s) for their contribution to the peer review of this work. A peer review file is available.

Reprints and permissions information is available at http://www.nature.com/reprints

Publisher's note Springer Nature remains neutral with regard to jurisdictional claims in published maps and institutional affiliations.

Open Access This article is licensed under a Creative Commons Attribution-NonCommercial-NoDerivatives 4.0 International License, which permits any non-commercial use, sharing, distribution and reproduction in any medium or format, as long as you give appropriate credit to the original author(s) and the source, provide a link to the Creative Commons licence, and indicate if you modified the licensed material. You do not have permission under this licence to share adapted material derived from this article or parts of it. The images or other third party material in this article are included in the article's Creative Commons licence, unless indicated otherwise in a credit line to the material. If material is not included in the article's Creative Commons licence and your intended use is not permitted by statutory regulation or exceeds the permitted use, you will need to obtain permission directly from the copyright holder. To view a copy of this licence, visit http://creativecommons.org/licenses/by-nc-nd/4.0/.

© The Author(s) 2024